

Epitaxial $\text{YBa}_2\text{Cu}_3\text{O}_{7-x}$ nanocomposite films and coated conductors from BaMO_3 ($M = \text{Zr}, \text{Hf}$) colloidal solutions

X Obradors¹ , T Puig¹, Z Li¹, C Pop¹, B Mundet¹, N Chamorro², F Vallés¹, M Coll¹, S Ricart¹, B Vallejo¹, F Pino¹, A Palau¹ , J Gázquez¹, J Ros² and A Usoskin³

¹ Institut de Ciència de Materials de Barcelona, ICMAB—CSIC, Campus UA Barcelona, E-08193 Bellaterra, Catalonia, Spain

² Departament de Química, Facultat de Ciències, Universitat Autònoma de Barcelona, 08193-Cerdanyola del Vallès, Catalonia, Spain

³ Bruker HTS GmbH, D-63755 Alzenau, Germany

E-mail: xavier.obradors@icmab.es

Received 6 October 2017, revised 19 January 2018

Accepted for publication 26 January 2018

Published 22 February 2018



Abstract

Superconducting nanocomposites are the best material choice to address the performance required in power applications and magnets working under high magnetic fields. However, it is still challenging to sort out how to achieve the highest superconducting performance using attractive and competitive manufacturing processes. Colloidal solutions have been recently developed as a novel and very promising low cost route to manufacture nanocomposite coated conductors. Well dispersed and stabilized preformance nanoparticle solutions are first prepared with high concentrations and then mixed with the $\text{YBa}_2\text{Cu}_3\text{O}_7$ metalorganic precursor solutions to generate colloidal solutions to grow the nanocomposite films. Here we demonstrate, for the first time, that non-reactive BaZrO_3 and BaHfO_3 perovskite preformed nanoparticles are suitable for growing high quality thin and thick films, and coated conductors with a homogeneous distribution and controlled particle size using this fabrication method. Additionally, we extend the nanoparticle content of the nanocomposites up to 20%–25% mol without any degradation of the superconducting properties. Thick nanocomposite films, up to $0.8 \mu\text{m}$, have been prepared with a single deposition of low-fluorine solutions using an ink jet printing dispenser and we demonstrate that the preformed nanoparticles display only a very limited coarsening during the growth process and so high critical current densities $J_c(B)$ under high magnetic fields. These films show the highest critical currents achieved so far based on the colloidal solution approach, $I_c = 220 \text{ A/cm}^2$ at 77 K and self-field, and they still have a high potential for further increase in the film thickness. Finally, we also show that nanocomposite $\text{YBa}_2\text{Cu}_3\text{O}_{7-\delta}\text{BaZrO}_3$ coated conductors based on an alternating beam assisted deposited YSZ buffer layer on stainless steel metallic substrates can be developed based on these novel colloidal solutions. Non-reactive preformed oxide perovskite nanoparticles are therefore very promising elements to further advance the colloidal solution approach in the implementation of low cost and high performance coated conductors for high magnetic field applications.

Keywords: nanocomposite, BaZrO_3 , BaHfO_3 , vortex pinning, colloidal film

(Some figures may appear in colour only in the online journal)

1. Introduction

The discovery of nanocomposite $\text{REBa}_2\text{Cu}_3\text{O}_7$ (REBCO, RE = rare earth or Y) coated conductors (CCs) has generated the second highest boost towards the achievement of high superconducting performance, making these materials competitive enough for all the conceived electrical power applications [1–5]. The first development was the generation of the CC concept itself, i.e. the possibility to achieve biaxial texture of REBCO films on top of properly designed metallic substrates [6–8]. The use of CCs at high magnetic fields and high temperatures requires the development of efficient vortex pinning strategies and so artificial pinning centers (APCs) need to be created [1–3, 9–13].

Most of the CC fabrication techniques available today rely on vacuum deposition techniques (pulsed laser deposition, e-beam evaporation) or chemical approaches such as metalorganic chemical vapor deposition [1–3, 5, 11, 13] where nanocomposite structures can be defined using the simultaneous deposition of elements leading to two different crystalline phases: REBCO and a non-superconducting phase (usually also epitaxial), which behaves as an APC. Strain engineering ideas are then used to generate and control the self-assembled nanostructures embedded in the REBCO films [9, 10, 14–17].

Chemical solution deposition (CSD) is a completely different approach where the solution composition and deposition parameters determine the final film thickness while film epitaxy is achieved during a separate growth process. A thorough understanding of the thermodynamic, kinetic, chemical and nanostructural driving forces determining the final features of these epitaxial films has been required to achieve high performance CCs fabricated by CSD approaches. The main advantage of the CSD approach is the intrinsic low equipment investment and running cost expenses while high performance is preserved, although it is a complex issue to estimate the final manufacturing cost of CCs and its impact on the development of electrical power systems [5, 12, 18–24]. The first development of solution based nanocomposites was made on the basis of using complex solution salts including YBCO precursors and those of the secondary phase; BaZrO_3 for instance [25, 26]. On the basis of these complex solutions it was demonstrated that during the growth step a spontaneous segregation of the secondary phase occurs leading to randomly distributed and essentially randomly oriented nanoparticles [25–32]. In these spontaneous segregated nanocomposites (ss-nanocomposites) the nanoparticles are *in situ* generated during the same heating step as that of the epitaxial YBCO film. The nanoparticles are usually formed slightly before the YBCO film during the heating step and so they are essentially randomly oriented. Several types of these secondary phase nanoparticles have been formed (BaZrO_3 , BaHfO_3 , Ba_2YTaO_6 , Y_2O_3 , Gd_2O_3 , etc) and a breadth of nanostructural features that positively influence the vortex pinning capability of these films and CCs have been demonstrated [21, 26–32]. A detailed analysis of the nanostructure–critical currents relationship in a wide range of compositions, however, has clarified that the secondary defects generated at the interfaces are associated with randomly

oriented nanoparticles or exhibiting axioepitaxy, i.e. having multiple fiber axis texture [27, 33, 34]. The most relevant defects are $\text{YBa}_2\text{Cu}_4\text{O}_8$ (Y248) intergrowths and it has been shown that they share the main responsibility for the sought APC effect, instead of the nanoparticles themselves being the pinning centers [27, 28, 35–38]. These planar defects consist of an intergrowth of an extra Cu–O chain layer inserted in the YBCO structure, which includes a high concentration of vacancies and which is surrounded by a partial dislocation generating intense local strains in the YBCO lattice [35, 36]. We suggested a novel vortex pinning mechanism to explain the role of nanostrain in the YBCO lattice by strong isotropic APCs in CSD derived nanocomposites, and how it deeply modifies the nanostructure of the YBCO films [27, 35, 36, 39]. Actually, optimizing the APC effect in HTS is a complex issue because the size and density of non-superconducting regions (nanoparticles or induced defects) should be in the range of the coherence length, but it also depends on vortex–vortex interaction and on the dimensionality and orientation of the multiple defects existing in YBCO films. The optimal non-superconducting fraction and dimension will depend, therefore, on temperature and magnetic field strength and orientation [40, 41].

Unfortunately, however, the CSD approach to nanocomposite films based on spontaneous segregation of the secondary phases has several intrinsic limitations when the size and distribution of the nanoparticles need to be properly controlled. For instance, it was clear that above a nanoparticle concentration of 10%–12% mol there is a strong tendency towards nanoparticle aggregation, which reduces the available cross section of the current path and thus the superconducting performance decreases. Several attempts have been made, however, to increase the capability of performing a fine tuning of the APC landscape through nanoparticle size control [27–29, 42–44].

For that reason, a completely new route to CSD nanocomposites has been recently developed: the colloidal solution approach [45], which has never been properly described before in any type of functional oxides. This approach consists in the preparation of preformed metal oxide nanoparticles with well-defined size and structure which are then mixed with the metalorganic precursor solutions used for CSD YBCO film growth to form a colloidal solution [46–49]. With these colloidal solutions the rest of the film growth process should remain essentially unchanged and so we could name the novel films derived from this process as ‘preformed nanoparticle nanocomposites’ (pn-nanocomposites) because the nanoparticles have been prepared prior to the YBCO film crystallization.

Following this methodology it should be possible, in principle, to achieve a tight control of the nanoparticles size and shape, as well as creating a homogeneous distribution of the nanoparticles and of the induced nanostructure within the YBCO lattice. Several difficulties, however, were described in our initial investigation of the colloidal solution approach [45–47, 50]. The main difficulties were associated with the following items: preserving the colloidal solution stability owing to the strong ionic character of the metalorganic

solutions; inhomogeneous distribution of the preformed nanoparticles during the deposition, pyrolysis or growth steps; chemical reactivity of the nanoparticles with the YBCO precursors during the growth step; coarsening of the nanoparticles during the high temperature annealing steps; aggregation of the nanoparticles induced during any of the processing steps; and poor control of the induced nanosstructure within the YBCO lattice. Several nanoparticle compositions have been described so far as part of the strategy of the YBCO colloidal nanocomposites: $M\text{Fe}_2\text{O}_4$ spinels ($M = \text{Mn, Co}$) [47, 48, 50], CeO_2 fluorite [45] and ZrO_2 fluorite [45, 46, 51]. In all these cases the chemical reactivity of the nanoparticles was detected leading to final modified secondary phases after growth: YBaCuFeO_5 , $\text{Ba}_3\text{YFeMnO}_9$ [47, 50], BaCeO_3 [45] and BaZrO_3 [45, 46, 51] are phases that have been identified. As a consequence of these complex chemical and structural transformations of the preformed nanoparticles into the new nanoparticles, it was found that keeping tight control on the final stoichiometry and nanosstructure of the nanocomposite YBCO films was problematic [45, 46]. It became clear then that it would be much more rewarding to prepare stable preformed nanoparticles that are non-reactive with the YBCO precursors and that can preserve the previously determined morphological features of the nanoparticles (size, shape) during the growth step of the YBCO films. As a consequence, the potential of the pn-nanocomposites to achieve a fine tuning of the APC is very appealing.

It is known that several compositions of binary or ternary oxide perovskite phases are chemically compatible with YBCO. We should mention, particularly, BaZrO_3 and BaHfO_3 perovskites, which lead to very promising results in the CSD spontaneous segregation approach (ss-nanocomposites) [25, 27, 30–32]. We have concentrated our efforts on creating a chemical solution approach to grow BaMO_3 ($M = \text{Zr, Hf}$) nanoparticles and then to stabilize them in the trifluoroacetate (TFA) precursor solution being used at present in most of the CSD approaches to CCs. These secondary phases have already been shown to induce vortex pinning centers when they are introduced in ss-nanocomposites [25, 27, 30–32, 52].

In this work, we report on the progress achieved so far in our novel methodology of nanocomposite film growth based on colloidal solutions. We have selected as non-superconducting nanoparticles the two perovskites, BaZrO_3 and BaHfO_3 , which are not reactive with the YBCO matrix. We will show for the first time that these perovskite phases can be indeed used as preformed nanoparticles, while the colloidal solution properties, the pyrolysis treatment and the nucleation and growth processes of the nanocomposite films remain essentially similar to that of pristine YBCO. Furthermore, we will also show that the pn-nanocomposite methodology allows achieving higher control of the nanoparticle size and of distribution homogeneity and much larger nanoparticle concentrations can be used while keeping high superconducting performance of the nanocomposites.

In order to increase the YBCO film thickness, and so the total critical current I_c , using the CSD approach, as well as making feasible the industrial scaling of CC production, the ink jet printing (IJP) approach for solution deposition has been recently developed. This technique requires modified low-fluorine solutions, i.e. solutions where some of the Y, Ba and Cu salts do not necessarily include fluorine [53–55]. A reduction of ~80% of F content in the solution has been demonstrated to lead to very similar YBCO superconducting performance [54]. These novel low-fluorine solutions have been used here to grow thick YBCO nanocomposite films. Overall, an enhanced effectiveness in the vortex pinning properties has been demonstrated for all the films and CCs reported here and so we provide strong support to the idea that CSD based CCs have strong potential as a low cost route to high performance coated conductors.

2. Experimental

2.1. Nanoparticle synthesis and characterization

Various synthetic methods are available to prepare metal oxide nanoparticles [56, 57]. Here we will focus on solvothermal synthesis, using environmentally friendly solvents, e.g. benzyl alcohol, triethylenglycol, isopropanol, ethanol and water [48]. This is an interesting technique for large scale production compared to the previously published microemulsion approach [58], which shows a more limited capability to adapt to different nanoparticle compositions.

BaMO_3 ($M = \text{Zr, Hf}$) nanoparticles were synthesized using thermal activation, starting from $\text{Ba}(\text{OH})_2$ and $\text{Zr}(\text{OBu})_4$ or $\text{Hf}(\text{OBu})_4$ ($\text{Bu} = \text{butoxide}$) as molecular precursors in TEG/EtOH and ammonium hydroxide. The precursor was treated at 180 °C at different times (in the range 1–20 h) in a sealed reactor, leading to cubic crystalline BaZrO_3 and BaHfO_3 nanoparticles with well-defined facets, typical sizes of 10 nm for BaZrO_3 and 7–8 nm for BaHfO_3 (inset to figure 1(a)) and without any sign of nanoparticle agglomeration, as was observed in previous works [59]. The nanoparticles obtained had functionalized surfaces and thus yielded to a stable colloidal solution with non-agglomerated nanoparticles in alcoholic media (e.g., methanol, ethanol, butanol) [45, 46, 60]. The size and distribution of nanoparticles were evaluated by means of transmission electron microscopy (TEM) and dynamic light scattering (DLS) analysis. High resolution TEM (HRTEM) micrographs were obtained on a 200 kV JEOL 2011 TEM, which has a resolution point of 1.8 Å at 200 kV. The crystal structure of the nanoparticles was verified by x-ray diffraction using x-ray powder diffraction studies (XRD) performed on a D5000 Siemens x-ray powder diffractometer in reflection mode using Cu-K_α ($\lambda = 1.5406 \text{ \AA}$) radiation. Both, HRTEM and XRD confirmed the good crystallinity of the nanoparticles and the cubic perovskite structure (figures 1(a) and (b)). A Zetasizer Nanoseries Nano-ZS instrument (Malvern Instruments, UK) was used for DLS measurements. DLS analysis yielded a

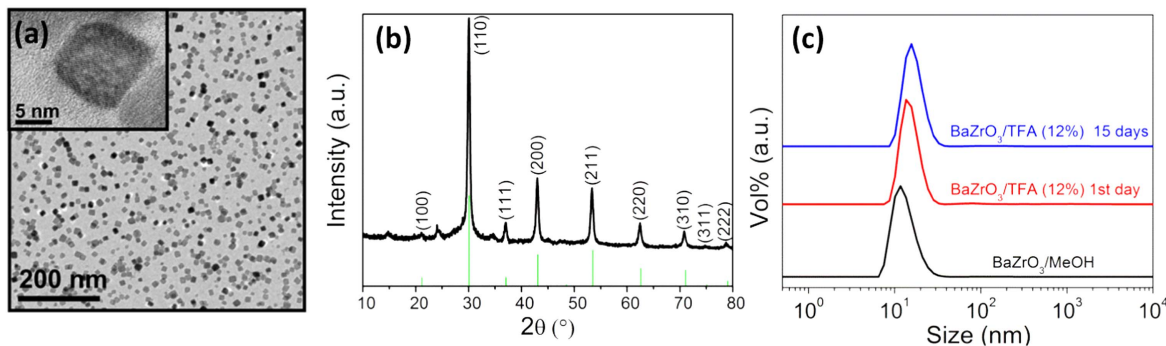


Figure 1. (a) TEM image of BaZrO_3 nanoparticles prepared by solvothermal synthesis. Inset: HRTEM view of a nanoparticle where a high crystalline quality is appreciated together with well-defined faceting. (b) XRD pattern of the BaZrO_3 nanoparticles confirming the cubic perovskite structure. (c) DLS spectra of a BaZrO_3 nanoparticles solution and a TFA-YBCO– BaZrO_3 colloidal solution with 12% mol BaZrO_3 .

solvodynamic diameter of 10–12 nm and 7–8 nm, for BaZrO_3 and BaHfO_3 , respectively, for the steric stabilized nanoparticles in methanol (figure 1(c)), thus confirming that no nanoparticle agglomeration occurs.

2.2. YBCO colloidal solutions and deposition

The preparation of TFA-YBCO solution consisted in the dissolution, in an inert atmosphere, of YBCO powder in an excess of trifluoroacetic anhydride, a small quantity of trifluoroacetic acid (Aldrich 99%) as catalyst and recently distilled acetone as solvent. The mixture was stirred and heated at 50 °C for 72 h. The resulting solution was filtered and evaporated through vacuum. The mixture of TFA salts ($\text{Ba}(\text{TFA})_2$, $\text{Cu}(\text{TFA})_2$ and $\text{Y}(\text{TFA})_3$) was then dissolved in sufficient anhydrous methyl alcohol or dry acetone to give a solution with a total metal ion concentration of 1–1.5 M [61]. This solution was stored in sealed vials, in an inert atmosphere. The viscosity was measured with a Haake RheoStress 600 rheometer reaching values of 2–5 mPas. The metal stoichiometry was confirmed by titration analysis and the water content was evaluated using the Karl–Fischer method to be always <1 wt%.

The low-fluorine precursor solution used to deposit the thick YBCO nanocomposites was prepared by dissolving the acetates (Ac) of anhydrous copper and barium ($\text{Cu}(\text{OAc})_2$ and $\text{Ba}(\text{OAc})_2$), and anhydrous yttrium trifluoroacetate ($\text{Y}(\text{TFA})_3$ anhydrous) in methanol and propionic acid [54]. The total concentration of metal ions was 1 M and the stoichiometry was kept $\text{Y}:\text{Ba}:\text{Cu} = 1:2:3$. The solution was then filtered and stored in sealed vials. Just before the deposition through the ink jet dispenser a 6% v/v of an additive of polymer compound (Kao Chimigraf, Barcelona, Spain) and 5% mol $\text{Ag}(\text{TFA})$ was dissolved in the low-fluorine precursor solution.

Colloidal stabilization in TFA-YBCO molecular precursor solutions is not straightforward, since the precursor exhibits an alcoholic and highly ionic environment due to the Y, Ba, Cu metal salts. For the preparation of the colloidal solutions containing different concentrations of nanoparticles, adequate volumes of alcoholic solutions of the BaMO_3 ($M = \text{Zr}, \text{Hf}$) nanoparticles were added to the previously

prepared TFA or low-fluorine solutions and the final stability was checked in time by means of TEM and DLS analysis.

The BaZrO_3 and BaHfO_3 nanoparticles, stabilized with triethyleneglycol in methanol, obtained via solvothermal synthesis, can be introduced into the methanol-based TFA-YBCO precursor solution up to 24% mol. DLS measurements (figure 1(c)) confirmed the presence of individual nanoparticles in suspension, with a solvodynamic diameter of about 15–20 nm due to the high ionic environment. The suspensions remained stable for more than three weeks (the peak shift in DLS performed at different times after stabilization of the colloidal solutions was ~20%, see figure 1(c)), thus indicating that no nanoparticle agglomeration occurred, which would lead to a double peak structure in the DLS pattern. Similar behavior was observed for low-fluorine solutions; in this particular case, due to the blue color of the colloidal ionic solutions, the DLS study was performed using a white solution where copper salts were substituted by zinc salts. All these colloidal solutions lead to homogeneous pyrolyzed films, as reflected by optical microscopy observations.

Colloidal solutions prepared using TFA precursors were used for thin film deposition based on a spin coating approach. The typical acceleration and speed parameters used in this case were 6000 rpm s⁻¹ and 6000 rpm for 2 min and the final film thickness after growth was in the range of ~150 nm for a single deposition [61]. In some cases three depositions were made with intermediate pyrolysis processes, leading to a final film thickness of ~350 nm.

Low-fluorine solution precursors were prepared to be used in a home-made ink jet printing system with a piezoelectric single nozzle (from Microfab Technologies Inc.) with a diameter of 60 μm . The dispenser was able to eject drops with a radius around 20 μm with a volume around 70 pl. Therefore, single deposition of those drops led to a final film thickness of 0.8–1.0 μm while a double deposition allowed reaching films of at least 1.6 μm .

2.3. YBCO nanocomposite films and coated conductor growth

The growth of YBCO nanocomposites was addressed using the following architecture. First of all, a pristine YBCO seed layer was fabricated though spin coating deposition

of a highly diluted pristine TFA-YBCO solution (0.3 M of metallic ion concentration) on LaAlO₃ (LAO) single crystal substrate (5 mm × 5 mm) or metallic substrates (^{CSD}CZO/^{ABAD}YSZ/SS), where ABAD = alternating beam assisted deposition [62, 63] and Ce_{0.9}Zr_{0.1}O_{3-y} (CZO) is a cap layer grown by CSD. The YBCO layer was subjected to a standard pyrolysis process [64] performed in O₂ atmosphere. The growth of CZO cap layers (~20 nm thick) on ^{ABAD}YSZ/SS metallic substrates was performed following a previously described process [55, 65]. When the YBCO seed layer was used to grow thick nanocomposites the composition was modified with an additional 5% mol Ag using the corresponding Ag(TFA) salts [9, 66]. Next, YBCO–BaMO₃ (*M* = Zr, Hf) colloidal precursor solutions were deposited on the as-pyrolyzed YBCO buffered substrate using spin coating in the case of TFA precursors and using IJP in the case of low-fluorine precursors. The low-fluorine solution concentration for IJP was 1 M and a single deposition was used for a final film thickness of ~0.8 μm.

The pyrolysis process was slightly different in the case of TFA precursors (maximum temperature 310 °C) [64, 67] than in the case of low-fluorine precursors (maximum temperature 500 °C) [54]. Subsequently, the YBCO–BaMO₃ (*M* = Zr, Hf) nanocomposite solid precursor films were crystallized at temperatures ranging from 770 °C to 820 °C for 150 min in P_{O₂} = 2 × 10⁻⁴ atm with P_{H₂O} = 2.3 × 10⁻² atm in the case of thin films and P_{H₂O} = 0.2 atm for thick films. The heating rate during the growth process was kept at 25 °C min⁻¹. Finally, the superconducting YBCO phase was obtained by oxygen annealing at 450–550 °C and P_{O₂} = 1 atm for 210 min.

The architecture of the thick nanocomposite coated conductors achieved in this work was ^{CSD}YBCO/^{CSD}CZO/^{ABAD}YSZ/SS. Bruker provided the metallic tapes of stainless steel (SS) with YSZ on top deposited by ABAD [62, 63]. The non-magnetic SS metallic tapes were 4 mm wide and 0.1 mm thick. The CZO buffer layers were deposited by spin coating and grown in air atmosphere at 900 °C for 60 min. The thick YBCO layers were then deposited by IJP and pyrolyzed in the same conditions as thick YBCO layers on LAO substrates, including the seed layer. The crystallization of these samples was performed in a tubular furnace at 750 °C with P_{O₂} = 2 × 10⁻⁴ atm and P_{H₂O} = 0.2 atm.

2.4. Structural and physical characterization of the films

The crystalline phases and texture analyses of the fully converted YBCO nanocomposite films were conducted by XRD using a Bruker AXS GADDS diffractometer equipped with a 2D detector. The *c*-axis crystallographic alignment quality was quantified by the analysis of the full width at half maximum (FWHM) of YBCO (005) obtained through rocking curve (ω-scan) measurements conducted using the Siemens D5000 diffractometer with Cu-K_α (λ = 1.5418 Å). The strain of the films was quantified based on the Williamson–Hall method by analyzing the symmetric (001) Bragg diffraction integral breadth acquired in a Siemens D5000 diffractometer using Cu-K_α radiation. From the Williamson–Hall plots we

could determine the rms microstrain parameter ε and associate it with the defect structure of the YBCO films [25, 66].

The surface morphology of the final YBCO films was studied using a scanning electron microscopy (FEI Quanta 200 FEG). The nanoparticle distribution, size and atomic scale defect landscape of the YBCO nanocomposites were investigated by scanning transmission electron microscopy (STEM) using an FEI Titan 60–300 microscope equipped with an X-FEG gun, a CETCOR probe corrector and a Gatan TRIDIEM 866 ERS energy filter operated in STEM mode at 300 kV. The critical current density (J_c) and superconducting transition temperature (T_c) were obtained inductively from hysteretic magnetization and low field zero field cooling (ZFC) magnetization measurements performed with a superconducting quantum interference device (SQUID) magnetometer (Quantum Design, San Diego, CA). Critical current densities were calculated accordingly with the Bean critical state model of thin disk [68, 69]. Transport measurements were performed in a physical property measurement system Quantum Design system provided with a 9 T magnet and variable temperature from 5 to 300 K, to obtain the critical current density $J_c(T, B, \theta)$. The standard four probe method was used for the transport measurement in patterned films with narrow bridges of 200 μm in length and 10 to 80 μm in width. The details of the specimen patterning and transport measurement process have been introduced in previous reports [27].

3. Results and discussion

3.1. Growth of nanocomposite films

Heteroepitaxial nucleation is a subtle phenomenon that is grounded on thermodynamic and kinetic effects and so in CSD grown multilayers several parameters may influence the crystalline orientation of the first stable nuclei, as well as the nuclei density. Our recent work on YBCO nanocomposites has shown that depending on the nanoparticles size and concentration, as well as of the YBCO film thickness, the nucleation process may be strongly modified [45, 46]. Therefore, the first issue to be solved is to determine how to achieve an accurate control of the supersaturation conditions of YBCO film formation because this is the main parameter determining the heterogeneous nucleation process at the substrate interface. Once the conditions for *c*-axis nucleation have been identified, the film growth conditions need also to be properly established for large thicknesses. Here we report first how to achieve a tight control of the nucleation and growth processes in thin and thick YBCO films on single crystalline substrates and then on metallic substrates suitable for coated conductor fabrication.

3.1.1. Nucleation and growth of nanocomposite thin films. In previous works, it was shown that the heterogeneous *c*-axis oriented nucleation of YBCO films on single crystalline substrates may be perturbed when nanocomposite films are grown [45, 46]. This is mainly due to the fact that an

excessive concentration of secondary phases may be accumulated at the interface and then, due to the large lattice mismatch of YBCO with these nanoparticles (BaZrO_3 and BaHfO_3 for instance), other crystalline orientations may also nucleate, thus perturbing the texture quality of the films. This difficulty could be overcome by using pristine YBCO seed layers at the substrate interface. A single layer of pyrolyzed YBCO films (thickness in the range of 25–50 nm) was shown to be effective to overcome this difficulty [27, 45, 46]. On top of this layer the nanocomposite films develop a robust homoepitaxial growth and preserve a high quality film texture. We attribute this effect to an enhanced effectiveness of the homoepitaxial growth of YBCO– BaMO_3 ($M = \text{Zr, Hf}$) nanocomposites, which may retain high quality even when the percentage of available YBCO interface (seed layer) is reduced at high concentration of preformed BaMO_3 ($M = \text{Zr, Hf}$) nanoparticles [27, 45, 46].

In the present case we have followed this strategy when using the preformed BaMO_3 ($M = \text{Zr, Hf}$) nanoparticles. Both in the case of TFA-YBCO solutions (spin coated thin films) and in the case of low-fluorine thick YBCO films on single crystalline and metallic substrates (IJP thick films), we have previously deposited a YBCO pristine seed layer about 50 nm thick.

In the case of TFA-YBCO nanocomposite films we concentrated on investigating the influence of the nanoparticle concentration and size on the final film homogeneity and its influence on the superconducting properties. We found that using BaMO_3 ($M = \text{Zr, Hf}$) nanoparticles with an initial diameter in the range 5–10 nm the YBCO films keep the *c*-axis nucleation up to 20%–25% mol (figures 2(a)–(d)). This compositional range goes well beyond that previously achieved based on the spontaneously segregated approach where strong texture degradation appeared beyond about 10%–12% mol [27, 28]. Actually, here the role of the pristine YBCO seed layer to extend the nanocomposite compositional range was found to be very important. This is clearly seen in figures 2(c) and (d), where we report SEM images of YBCO– BaZrO_3 20% mol films with a thickness of ~ 150 nm, with or without a pristine YBCO seed layer. Our results show that epitaxial growth is only achieved when a YBCO seed layer is used. This strategy appears, therefore, very attractive to reach high concentrations of BaMO_3 ($M = \text{Zr, Hf}$) nanoparticles in the pn-nanocomposite films.

The growth conditions of films with different nanoparticle concentrations (up to 25% mol) and nanoparticle sizes (5–10 nm initial mean diameter) were investigated for both BaZrO_3 and BaHfO_3 compositions. Although the typical film thickness achieved with a single spin coating deposition was ~ 150 nm, similar results were obtained through multideposition (three times) where films in the range ~ 350 nm were achieved.

The most outstanding result is that no special heat treatments were required to achieve nanocomposites that preserve a high texture and crystallinity quality up to nanoparticle content of 25% mol, for both nanoparticle compositions. This was demonstrated through 2D GADDS XRD patterns and SEM images showing that a very limited

porosity remains after growth (figure 2(c)). Additional ω -scans of (001) peaks from the XRD patterns showed that fully grown nanocomposite films have a similar epitaxial quality to pristine films ($\Delta\omega \sim 0.5^\circ$). Typical nanostrain values for YBCO–20% mol BaZrO_3 and BaHfO_3 nanocomposites were $\varepsilon = 0.18\%$ and $\varepsilon = 0.20\%$, respectively, which are consistent with those previously observed in other ss- and pn-nanocomposites [27, 45, 46]. STEM images of typical large content nanocomposite films are displayed in figures 3(a)–(d). The low resolution STEM images show that the nanoparticle size and their distribution within the films are fairly homogeneous. The typical final diameters of the nanoparticles are in the range 10–20 nm, very close to the initial mean diameter of ~ 10 –12 nm. Only a few nanoparticles appear to have dimensions above this range, thus suggesting that nanoparticle coarsening occurs during the growth process. At the present stage it is still not possible to perform a more quantitative analysis of the final size of the nanoparticles within the nanocomposites owing to the fact that STEM images have a tendency to statistically minimize the weight of the smallest diameters in the distribution patterns. In any case, it is remarkable that a high degree of nanoparticle homogeneity (monodisperse collection) was achieved through our process at this high nanoparticle concentration. This demonstrates that the strong tendency for nanoparticles to agglomerate (polydisperse collection) previously detected in ss-nanocomposite films can be avoided [28]. It is also remarkable that the previously described sources of inhomogeneity in pn-nanocomposite films [45, 46], such as CeO_2 nanoparticles pushing to the surface or nanoparticle accumulation at the interface for ZrO_2 nanocomposites, was completely avoided here with our novel preformed nanoparticle approach. Concerning the nanoparticle orientations, our STEM analysis suggests that they are mainly randomly oriented, although an axiotaxy texture, as recently characterized for BaCeO_3 nanoparticles, cannot be excluded at the present stage [33, 34]. The behavior of well dispersed BaMO_3 ($M = \text{Zr, Hf}$) nanoparticles appear, therefore, as the most promising to develop nanocomposite coated conductors with well controlled nanostructures and enhanced vortex pinning properties.

3.1.2. Nucleation and growth of nanocomposite thick films.

Once we established that YBCO nanocomposite thin films could be properly grown from colloidal solutions, we concentrated on developing thick nanocomposite films using IJP as a solution deposition approach. The final targeted film thickness range for a single deposition was 0.7–1.2 μm , although here we will report our analysis only in nanocomposite films with thickness ~ 0.7 –0.8 μm , even if we have already demonstrated that films with thicknesses up to 1.2 μm can be achieved in a single deposition. All films generated by IJP were based on the use of recently developed low-fluorine solutions [54], owing to their enhanced robustness and chemical stability versus H_2O absorption [70]. The nucleation and growth paths of low-fluorine YBCO films have been recently described [54]. Here we extended this research to the growth of thick nanocomposite

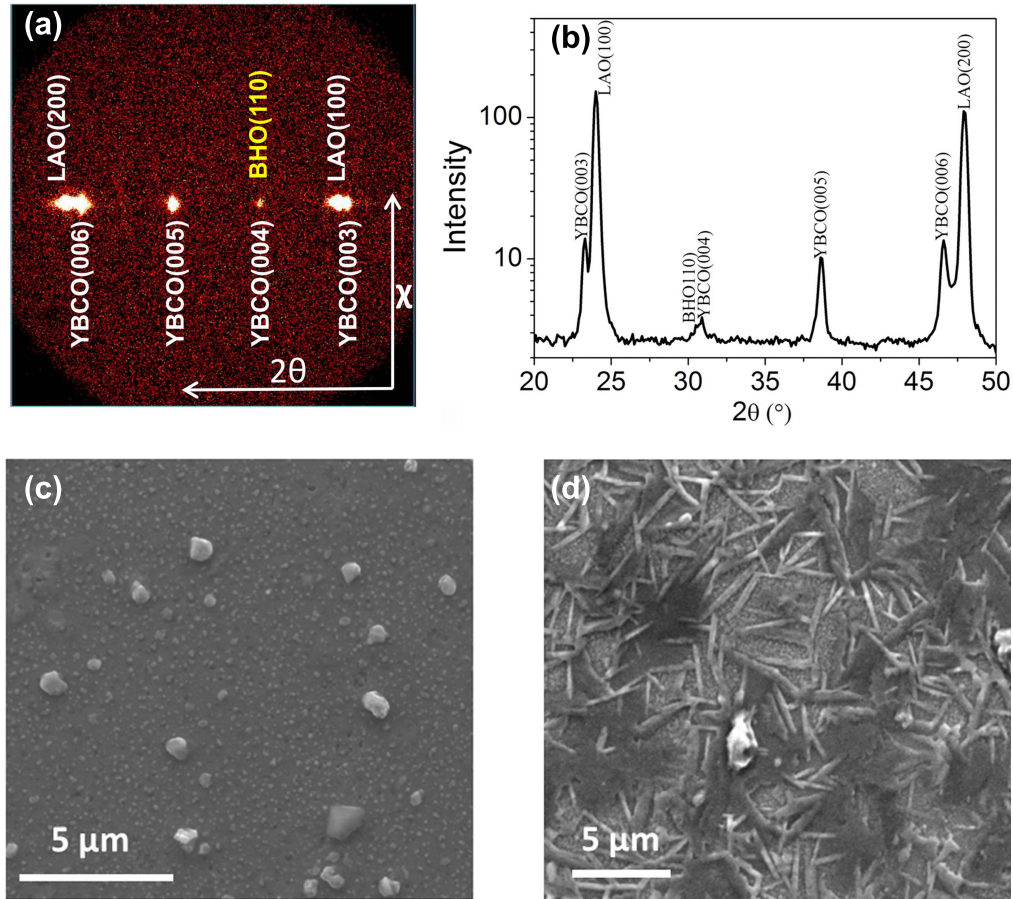


Figure 2. (a) 2D GADDS x-ray diffraction patterns of TFA-YBCO nanocomposite films with 20% mol BaHfO₃ (film thickness of ~150 nm) grown on a LAO substrate using a YBCO seed layer of 50 nm. (b) Integrated spectra from the XRD pattern of (a). (c) and (d) SEM images of the TFA-YBCO–BaZrO₃ (20% mol BaZrO₃) nanocomposite thin film samples grown with and without an YBCO seed layer, respectively.

films. The essential modifications required when YBCO thick films are grown through the BaF₂ route (TFA or low-fluorine precursors) are those related to the control of YBCO heterogeneous nucleation at the interface. As has been previously described [12, 66, 71], achieving *c*-axis nucleation of YBCO requires establishing low supersaturation conditions [72], while increasing the film thickness generates higher supersaturation conditions at the interface due to an enhanced gas impedance, which limits HF diffusion towards the surface after YBCO formation [12, 71, 73]. To compensate for this effect requires either to reducing the local HF pressure P_{HF} at the interface (through a reduced total pressure P_T which increases the gas diffusion, or through an increase of water pressure P_{H2O}) [12, 73, 74]. Another alternative is to modify the YBCO solution composition, for instance through Ag doping [12, 66, 75]. Here we have followed a combined approach, i.e. we have used a modified low-fluorine YBCO solution, which, in addition to BaMO₃ ($M = \text{Zr, Hf}$) preformed nanoparticles, 5% mol of Ag(TFA) was added, while we also increased P_{H2O} during the nucleation and growth processes. The role of Ag additives to promote *c*-axis nucleation at a given temperature was recently associated with a decrease in the decomposition temperature of YBCO with small amounts of Ag substitution [12, 66, 75]. This in turn results in a wider temperature window where *c*-axis nucleation is preserved. Figures 4(a), (b) and (d) show typical

XRD and SEM images of low-fluorine YBCO–BaMO₃ ($M = \text{Zr, Hf}$) nanocomposite films grown using some amount of Ag additives (~5% mol Ag(TFA)). Notice that a high quality *c*-axis texture was achieved under the selected conditions. This is in clear contrast to low-fluorine YBCO–BaMO₃ ($M = \text{Zr, Hf}$) nanocomposite films grown under the same conditions without Ag additives, where the (001) Bragg peaks are much broader in the 2D GADDS XRD pattern, thus confirming a strong texture degradation (figure 4(c)).

To complete the growth of the whole film thickness one can in principle use different processing conditions during the nucleation and growth steps [12, 28, 42, 76, 77]. This usually allows controlling separately the supersaturation conditions during nucleation (determining the crystalline orientation) from the growth step conditions of the rest of the film (determining the growth rate). For the sake of simplicity, however, in the present case we have used a unified approach, i.e. a single set of processing conditions has been used when films with a thickness of ~700–800 nm are investigated. Typically, the growth temperature was 770 °C and the gas pressures $P_{O_2} = 3 \times 10^{-4}$ bar, $P_T = 1$ bar and $P_{H2O} = 0.2$ bar. Typical XRD patterns and SEM images of nanocomposite films with 12% mol BaZrO₃ nanoparticles are displayed in figures 4(a)–(d). As is observed, the texture quality of the nanocomposite films is fully preserved (no

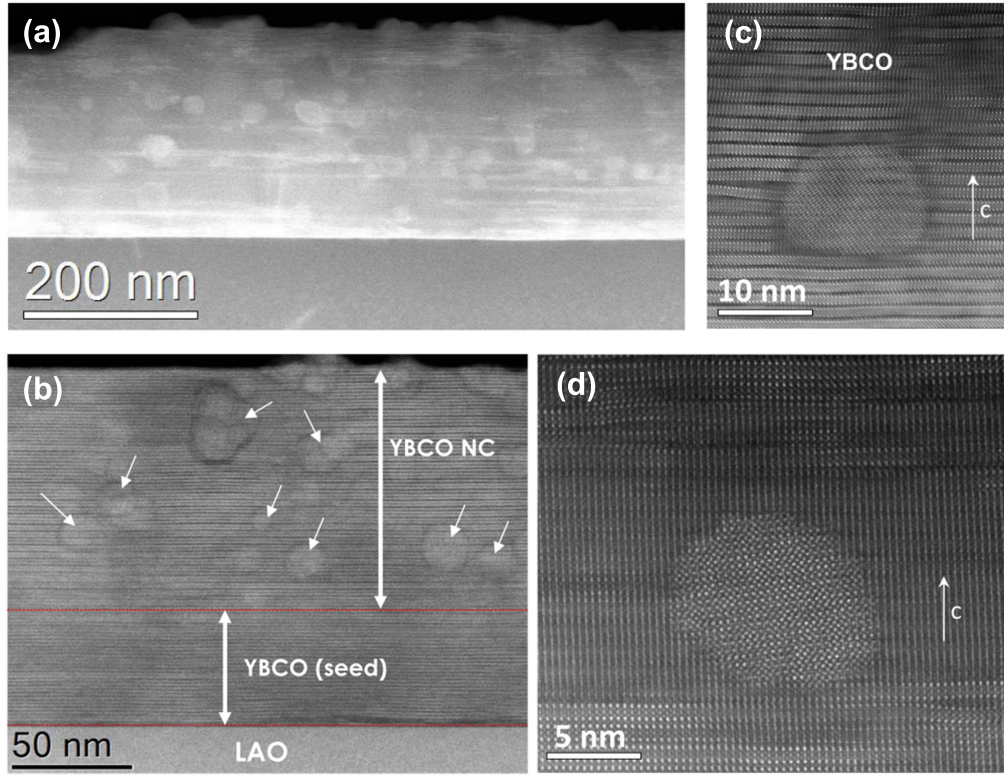


Figure 3. (a)–(d) STEM images of YBCO nanocomposite films with 20% mol of BaZrO_3 or BaHfO_3 nanoparticles grown from TFA precursors by spin coating. (a), (b) Low resolution STEM images with a general view of the films. (a) BaZrO_3 nanoparticles and (b) BaHfO_3 nanoparticles. Arrows in (b) point to the BaHfO_3 nanoparticles. A homogeneous nanoparticle distribution is observed. (c), (d) High resolution STEM images of the YBCO matrix around BaZrO_3 nanoparticles where a high density of stacking faults can be observed.

(103) Bragg peak is observed) and only a small increase in the ω -scan width of the (001) Bragg peaks was observed ($\Delta\omega = 0.8^\circ$). STEM analysis of the microstructure of these thick films shows that the nanoparticle size and distribution remain similar to that observed in thinner films (see figures 4(e), (f)). It is particularly appealing that the nanoparticle size does not appear to be modified when such new processing conditions are used, which suggests that they have robust stability during the different YBCO film growth conditions (temperature, growth rate, annealing time, etc.). We should remark, however, that wide area STEM images show that some residual porosity, or even secondary phases, still remain under the processing conditions used for thick films and so further refinement of these conditions is required.

As a final remark, concerning the nanocomposite thin and thick film nanostructure, we would like to note that in all films a high concentration of induced defects within the YBCO matrix was observed, i.e. the layered stacking faults parallel to *ab* planes and corresponding to the Y248 structure, as has been previously analyzed in detail [27, 35, 36]. As is observed in figures 4(e) and (f), the local nanostructure around the nanoparticles of films grown from low-fluorine precursors is very similar to that observed in films grown using TFA (figures 3(a)–(d)), even if their growth conditions differ. In particular, the randomness of the nanoparticle orientation previously discussed in TFA-based films is also observed here in low-fluorine films (figure 4(f)). Further analysis of the relationship between processing conditions

and the final nanostructure of the nanocomposite films, particularly nanostrain, will be required to achieve a well-defined path towards optimal superconducting properties. At the present stage, we can already conclude that the chemical stability of the small nanoparticles of BaMO_3 ($M = \text{Zr}, \text{Hf}$) is very favorable to developing nanocomposite films with large thicknesses and achieving well dispersed and homogeneously distributed nanoparticles.

3.1.3. Coated conductor: nucleation and growth on metallic substrates. Fabrication of CSD YBCO coated conductors based on ABAD metallic substrates was demonstrated recently using CZO as a cap layer (~ 20 nm thick) grown by CSD on top of ${}^{\text{ABAD}}\text{YSZ}/\text{SS}$ templates from Bruker and TFA-YBCO precursors [55, 65]. Here we have adapted the process to grow thick YBCO– BaZrO_3 nanocomposite films, as described in the previous section, to the ABAD substrates. The main difficulty in growing CSD based CCs is that of the interfacial chemical reactivity of CZO or CeO_2 cap layers with the BaF_2 precursors, which leads to the formation of some BaCeO_3 (BCO) at the interface [55, 65, 78, 79]. This perovskite has a large lattice mismatch with YBCO and hence, similar to the case of BaZrO_3 nanoparticle accumulation at the interface described in section 3.1.1, leads to undesired YBCO nucleation events and ultimately to a high concentration of randomly oriented YBCO grains. To avoid this limitation it is essential to define a process where the *c*-axis oriented YBCO grains nucleate faster than the

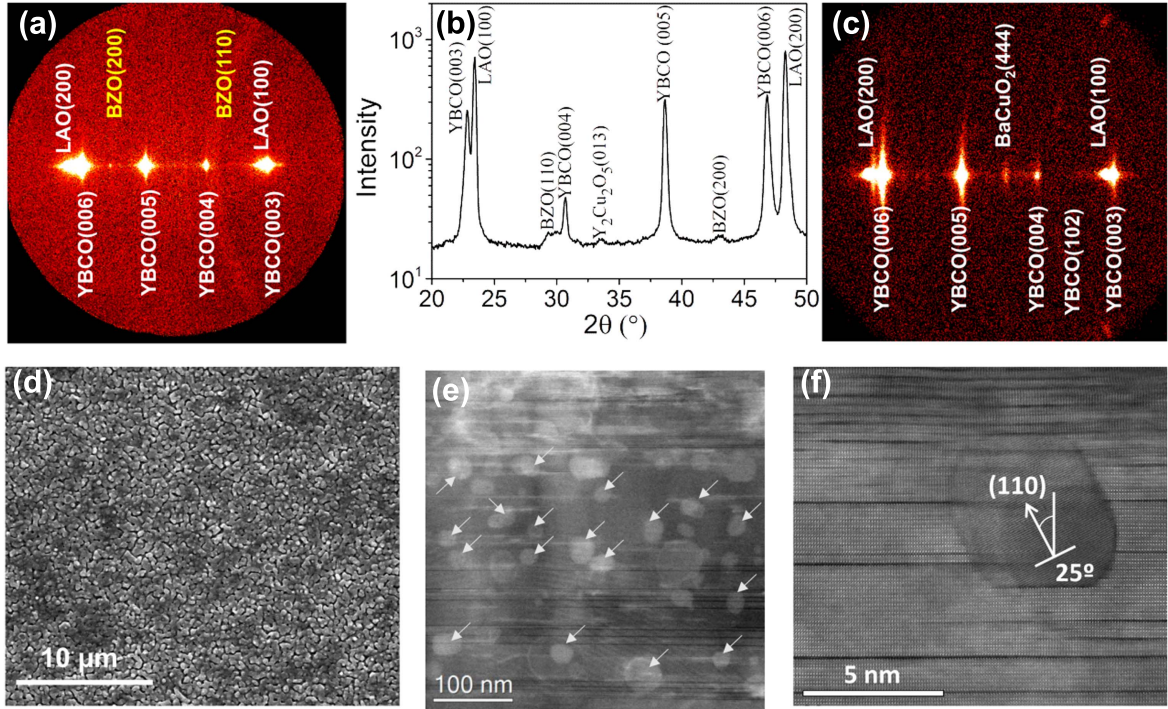


Figure 4. (a) 2D GADDS XRD pattern and (b) integrated spectra from the XRD pattern of (a) of a low-fluorine nanocomposite film YBCO–BaZrO₃ with 12% mol BaZrO₃ with a thickness of 850 nm and prepared by IJP deposition on a LAO substrate with an YBCO seed layer and using Ag(TFA) as additive. (c) 2D GADDS XRD pattern of the same film as (a) without using Ag as additive. (d) SEM image of the nanocomposite film described in (a) after growth. (e) STEM image of a 12% mol BaZrO₃ low-fluorine YBCO–BaZrO₃ film with a thickness of 850 nm where the BaZrO₃ nanoparticles are observed to be homogeneously distributed and the stacking faults are also generated around the nanoparticles. (f) High resolution STEM image of a non-epitaxial BaZrO₃ nanoparticle embedded in the YBCO matrix where a high concentration of stacking faults is observed.

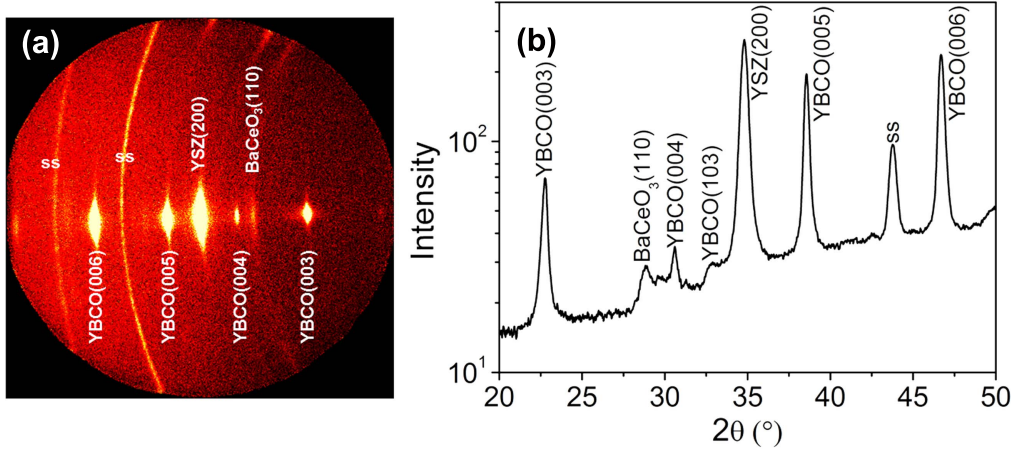


Figure 5. (a) and (b) 2D GADDS XRD patterns and integrated patterns of low-fluorine YBCO–BaZrO₃ nanocomposite (12% mol BaZrO₃) coated conductor grown on a^{CSD}CZO/^{ABAD}YSZ/SS metallic substrate (film thickness of ~700 nm). A YBCO seed layer of 50 nm was used.

formation of a BaCeO₃ interlayer. The best strategy to achieve this goal is, therefore, to reduce the growth temperature to keep as low as possible the interfacial chemical reactivity, although an optimum degree of supersaturation and the *c*-axis grain nucleation rate need to be preserved at the same time to keep a high texture quality [12, 71, 73, 76].

Here we report a single example of how the use of low-fluorine colloidal solutions, including the Ag(TFA) salt and

the BaZrO₃ nanoparticles, deposited by IJP, can lead to high quality nanocomposite CCs. The chosen preformed nanoparticles were BaZrO₃ with a starting diameter of about 10 nm, although the process is essentially valid for BaHfO₃ nanoparticles as well.

Figures 5(a) and (b) display 2D GADDS XRD patterns of a CC grown at 750 °C having a YBCO film thickness of ~700 nm (single IJP deposition), 12% mol BaZrO₃ nanoparticles and 5% mol Ag(TFA), which was grown on

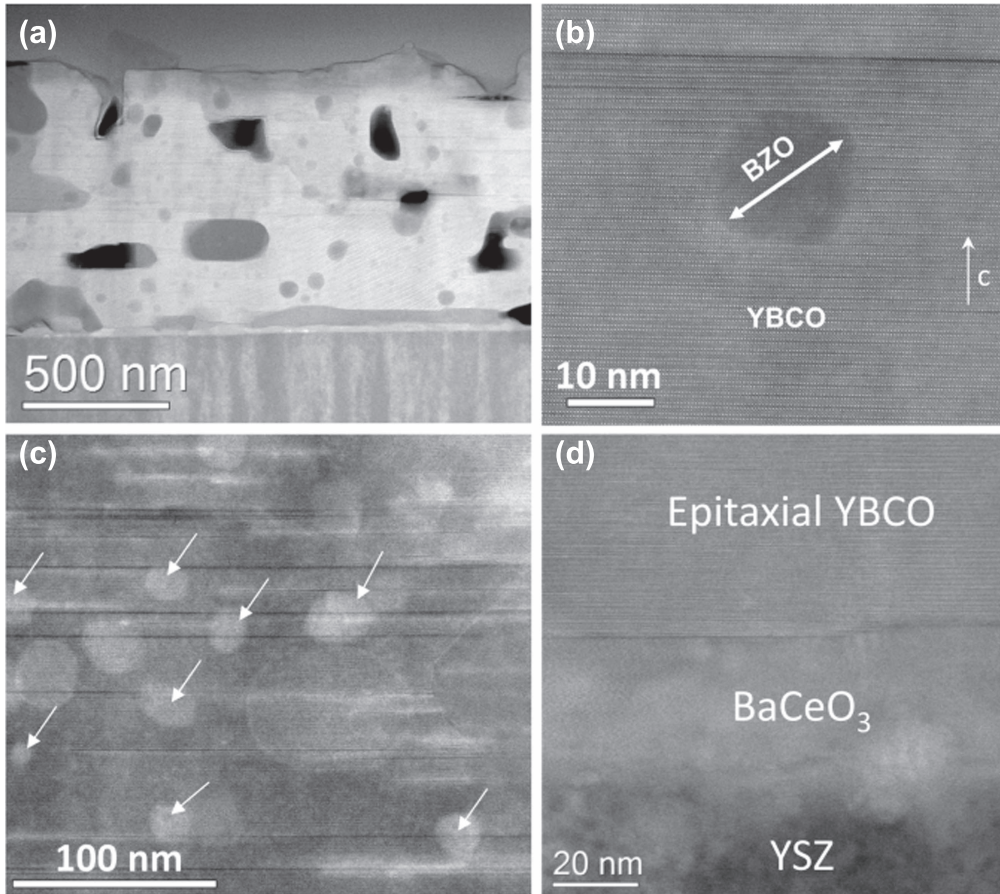


Figure 6. (a) Low magnification TEM image of a YBCO/^{CSD}CZO/^{ABAD}YSZ/SS nanocomposite coated conductor with a nanoparticle content of 20% mol BaZrO₃. (b)–(d) High resolution STEM images of the coated conductor described in (a) where the BaZrO₃ nanoparticles embedded within the YBCO matrix are indicated by arrows in (c) while (d) shows the interface with the buffer layer after being transformed to BaCeO₃.

top of a low-fluorine YBCO/Ag(TFA) film. As is seen in the integrated XRD pattern (figure 5(b)), the YBCO–BaZrO₃ nanocomposite coated conductor displays a complete *c*-axis texture (only a very weak signal of the randomly oriented grains (103) is observed), even if the CZO cap layer (~20 nm thick) has been fully transformed to BaCeO₃. This is further confirmed looking at the cross section STEM images displayed in figures 6(a)–(d) where the BaZrO₃ nanoparticles are indicated (arrows in (c)), together with the reacted BaCeO₃ cap layer in figure 6(d). Some residual porosity and typical secondary phases of the BaF₂ growth route (Y₂Cu₂O₅, BaCuO₂) are appreciated within the bulk of the YBCO layer in figure 6(a) [12, 26]. High resolution STEM images of BaZrO₃ nanoparticles indicate that the size and morphology remain similar to that observed on films grown on single crystal substrates (figure 6(b)) and that stacking faults are also generated in this case. Similar results were obtained when extending the nanoparticle content up to 20% mol BaZrO₃, as in the case of nanocomposites grown on top of LAO single crystals described in the previous section.

In conclusion, we have shown that the proposed growth process for colloidal solution based YBCO–BaZrO₃ pn-nanocomposites can be extended to the case of metallic substrates when proper consideration of the additional

complexities associated to the interfacial reactivity are taken into account. The followed strategy was to enhance the YBCO nucleation rate using Ag additives and choosing optimum supersaturation nucleation conditions.

3.2. Superconducting properties

In this section we will report the characterization of the superconducting properties of the different types of thin and thick nanocomposite films and coated conductors described in the previous sections, both those grown from TFA and low-fluorine metalorganic precursors.

The first common feature of all the films was that the superconducting transition temperatures could be kept as high as those of pristine films. Figure 7(a) displays one example of a low field ZFC magnetization measurement where the onset temperature is around 90 K and the transition width stays in the range 4–6 K in films with a high quality texture. The onset *T_c* values and transition widths were found to be constant up to the maximum film thickness tested so far, i.e. 1.2 μm, and for films with a BaMO₃ (*M* = Zr, Hf) content of 25% mol (figure 7(b)).

The second parameter that was systematically tested in our films was the self-field critical current density *J_c^{sf}*, which

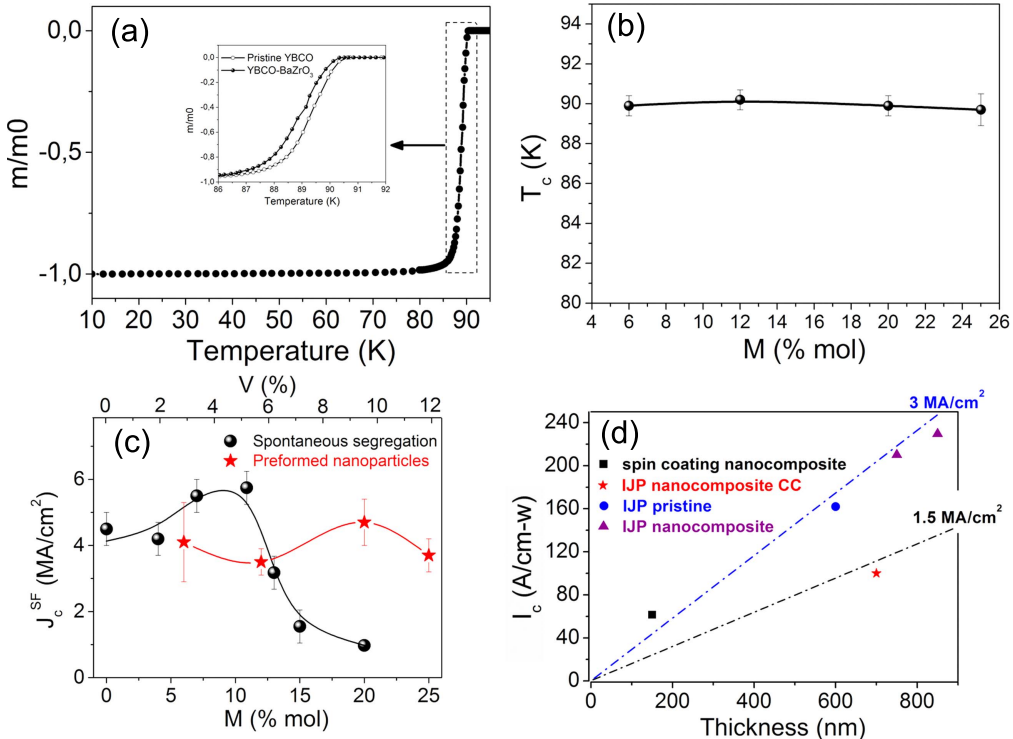


Figure 7. (a) Typical low magnetic field magnetization measurement of a YBCO nanocomposite film showing a sharp transition and a high T_c value. Inset: detail of the transition in a pristine and a TFA-YBCO–BaZrO₃ nanocomposite film. (b) Dependence of T_c determined inductively on the BaZrO₃ content in TFA-YBCO–BaZrO₃ nanocomposite films. (c) Dependence of J_c^{sf} (77 K) with the nanoparticle content in colloidal nanocomposite films (★), as compared to spontaneously segregated nanocomposite films (●). (d) Dependence of I_c (77 K) on the film thickness of colloidal nanocomposite films grown from TFA (spin coating) and low-fluorine colloidal solutions (IJP) and of a coated conductor (IJP). The nanoparticle content was either 12% mol or 20% mol BaZrO₃. The straight lines correspond to two different J_c^{sf} (77 K) values, as indicated.

was determined inductively through isothermal and temperature dependent SQUID magnetization measurements. Typical values of J_c^{sf} at 77 K in pristine YBCO CSD films were $\sim 3\text{--}4$ MA cm⁻² [12, 25, 27] and so we initially used this parameter to assess if the superconducting performance was preserved. Figure 7(c) reports, for instance, the dependence of J_c^{sf} , measured at 77 K for varying content of BaZrO₃ preformed nanoparticles in colloidal-based TFA-YBCO nanocomposite thin films. These values are compared to the corresponding YBCO–BaZrO₃ nanocomposite films obtained through the spontaneous segregation route (ss-nanocomposites) [27, 28]. It is clearly appreciated that the colloidal solution approach allows the preservation of high superconducting performance at higher nanoparticle concentrations. This reflects the enhanced homogeneity in the nanoparticle distribution discussed in the previous section.

Another very relevant parameter to assess the success in keeping high superconducting performance when increasing the film thickness is the dependence of $I_c = J_c^{sf}t$ with thickness t . Figure 7(d) displays the $I_c(t)$ dependence measured at 77 K for the different films described in the previous sections, together with two slopes corresponding to different J_c^{sf} values. It is seen that our nanocomposite films grown on LAO substrates keep fairly high J_c^{sf} values ($\sim 3\text{--}5$ MA cm⁻²) within the whole explored thickness range. The overall behavior confirms that no major differences exist in our

process when either TFA or low-fluorine precursors are used, nor in the solution deposition approach, i.e. spin coating or IJP. The tendency to a slight decrease in the critical current density at large film thickness ($J_c^{sf} \sim 3$ MA cm⁻²) was associated with the residual porosity and secondary phases still remaining when thick films are grown (figure 6). The highest I_c values achieved so far on LAO substrates and using IJP deposition were $I_c = 220$ A/cm-w at 77 K for a film ~ 850 nm thick. Concerning the corresponding coated conductors grown on top of ^{ABAD}YSZ/SS substrates and described in section 3.1.3, we can see that some decrease is still apparent in J_c^{sf} (~ 1.5 MA cm⁻²) when compared to films with the same thickness and so for a film ~ 700 nm thick we found $I_c \sim 100$ A/cm-w. This is mainly attributed to some increase of the concentration of the residual defects mentioned above (porosity and secondary phases), i.e. the percolating self-field critical currents are reduced due to the existence of some granularity effects [55].

The enhanced vortex pinning efficiency achieved through our novel colloidal solution approach to pn-nanocomposites using BaMO₃ ($M = \text{Zr, Hf}$) preformed nanoparticles has been tested through the analysis of the temperature and magnetic field dependences of $J_c(B, T)$ when $H//c$, as well as through analysis of the $J_c(\theta)$ anisotropy at constant magnetic field B [27, 80–82].

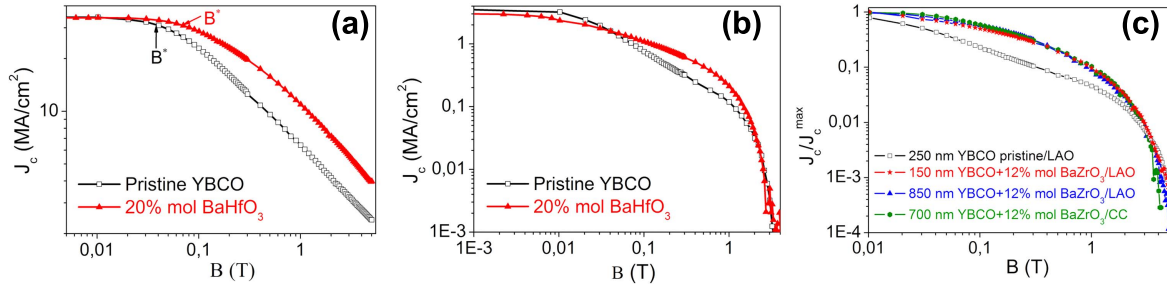


Figure 8. (a), (b) Magnetic field dependence of the critical current density $J_c(B)$ (SQUID measurements) of YBCO-BaHfO₃ nanocomposite thin films (20% mol BaHfO₃, TFA route and thickness of ~ 150 nm) compared with a pristine YBCO film. Measurements were performed at (a) 5 K and (b) 77 K. (c) Magnetic field dependence of the normalized critical current density $J_c(B)/J_c^{\max}$ (SQUID measurements at 77 K) of a 20% mol BaZrO₃ low-fluorine YBCO-BaZrO₃ nanocomposite coated conductor (^{CSD}CZO/^{ABAD}YSZ/SS substrate). Comparison is made with a YBCO pristine thin film and two YBCO-BaZrO₃ nanocomposite thick films with different thickness, as indicated, all of them grown on LAO substrates.

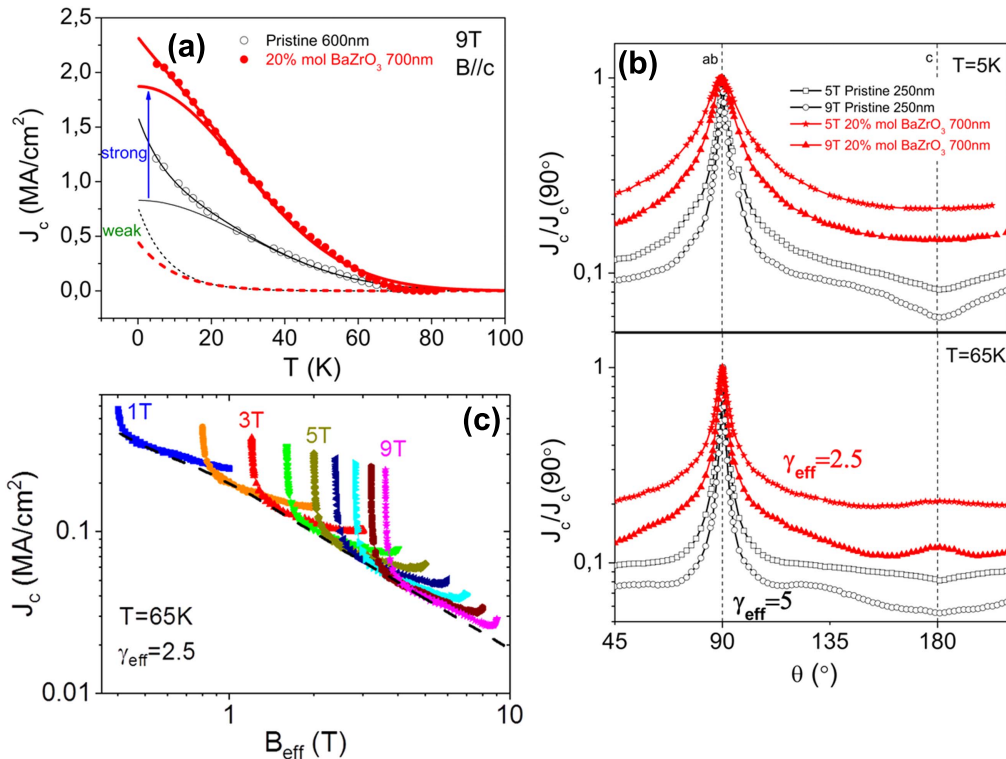


Figure 9. (a) Temperature dependence of the critical current density $J_c(T)$ obtained at 9 T by electrical transport measurements for a 700 nm thick low-fluorine YBCO-BaZrO₃ 20% mol BaZrO₃ nanocomposite film, as compared with pristine YBCO film with a thickness of 600 nm. These curves have been fitted with two contributions (strong and weak pinning) having different temperature dependences (see text). (b) Angular dependence of the critical current density $J_c(\theta)$ measured at 5 K and 65 K for a 20% mol YBCO-BaZrO₃ nanocomposite (~700 nm thick), as compared to a pristine film (~250 nm thick). (c) Scaling of the anisotropic behavior of $J_c(\theta, B)$ in the 700 nm thick low-fluorine YBCO-BaZrO₃ 20% mol BaZrO₃ nanocomposite film.

The first indication of an enhanced vortex pinning efficiency in the pn-nanocomposites comes from the isothermal $J_c(B)$ measurements reported in figures 8(a) and (b) corresponding to a YBCO-BaHfO₃ nanocomposite (20% mol) at 5 K and 77 K, respectively. As is clearly seen, the magnetic field dependence is smoothed when compared to the pristine YBCO samples. A parameter that reflects a continuous enhancement of the pinning efficiency is the crossover magnetic field B^* , i.e. the magnetic field where the low field single vortex pinning regime (detected through a plateau in the semi-log $J_c(B)$ dependence) switches to a higher slope,

usually towards a power law dependence characteristic of a collective pinning behavior (figures 8(a) and (b)) [29, 45, 46, 80]. The J_c decrease criterion for B^* determination was taken at the 90% level. Figure 8(a) indicates that, indeed, B^* is higher for the pn-nanocomposites (20% mol BaHfO₃ thin film) than for pristine YBCO films, i.e. $B^* \sim 38$ mT versus $B^* \sim 71$ mT at 5 K, respectively. Similar evidence for enhanced pinning was determined in coated conductors, as is observed in figure 8(c) reporting J_c measurements at 77 K (12% mol BaZrO₃), where a smoothed magnetic field dependence is observed when compared to a

pristine YBCO thin film while the smoothing is similar to that observed in nanocomposite thin films.

A second analysis that evidences an enhanced vortex pinning efficiency is the temperature dependence of $J_c(T)$. Figure 9(a) displays a comparison of this parameter, measured under a constant field of 9 T, for a nanocomposite thick film with 20% mol BaZrO₃ and a pristine YBCO film, both with thicknesses in the range of 600–700 nm. The $J_c(T)$ dependence can be decomposed into two contributions, strong and weak pinning contributions, which reflect the influence of different sorts of defects behaving as APCs and lead to a weaker and stronger temperature dependence, respectively [12, 80, 81]. In the present case, figure 9(a) shows that the highest pinning enhancement arises from the strong pinning contribution, although the weak pinning term is also positively influenced. This general behavior appears to be characteristic of solution derived nanocomposite films and it has been associated mainly with the increase of the nanostrain generated by a much higher stacking fault concentration in nanocomposite films [27, 80].

As a final indication of the success in enhancing vortex pinning in pn-nanocomposites, we include measurements of the anisotropic behavior of the critical currents $J_c(\theta)$. In figure 9(b) we report a comparison of measurements performed at 5 K and 65 K under magnetic fields of 5 T and 9 T for a pristine YBCO thin film and a pn-nanocomposite film with 20% mol BaZrO₃ (~ 700 nm film thickness). The overall behavior is similar to that of ss-nanocomposite films where $J_c(\theta)$ is described on the basis of isotropic and anisotropic pinning contributions where the second ones leads to $J_c(\theta)$ peaks associated with correlated disorder pinning centered at $B//c$ and $B//ab$ while isotropic pinning contributes to a broad background in $J_c(\theta)$ [25, 80, 83]. Concerning the anisotropic pinning contributions, notice the strong broadening of the $J_c(\theta)$ peak observed at $B//ab$ generated in the pn-nanocomposites. For instance, the FWHM values for $J_c(\theta)$ have been shown to be a useful phenomenological quantification of the effectiveness of planar defects as vortex pinning centers because they reflect the large accommodation angle characterizing the staircase regime of vortices near such defects [82, 83]. We observe, for instance, at 65 K and 9 T that the FWHM is in the range of $\Delta\theta \sim 4.8^\circ$ for pn-nanocomposites (already significantly larger than those observed in pn-nanocomposites based on ZrO₂ nanoparticles [45]). This peak broadening is attributed to an enhanced effectiveness of the stacking fault pinning and so our results confirm the conclusions achieved after a thorough STEM analysis of these pn-nanocomposites (section 3.1.2), which showed a high concentration of these planar defects.

An additional effect of the nanoparticles is that vortex channeling effects, signaled by a dip in the $J_c(\theta)$ curve at $H//c$ at 5 K (figure 9(b)), are suppressed in the pn-nanocomposites. Vortex channeling may occur in YBCO due to the existence of twin boundaries, which may behave as easy vortex flow channels, depending on the magnetic field, temperature or vortex motion direction [84, 85]. In solution derived YBCO ss-nanocomposite thin films we demonstrated

that the large concentration of stacking faults parallel to ab planes strongly reduced the vertical coherence of the twin boundaries and thus vortex channeling was deeply reduced [36, 85]. This is the reason for the suppression of the channeling effect and therefore of the $J_c(\theta)$ dip in the ss-nanocomposites. Here, we confirm that the same phenomenon occurs for the pn-nanocomposites, as reported in figure 9(b).

Finally, the anisotropic $J_c(\theta, B)$ values of YBCO films are characterized by an isotropic pinning contribution, which may be described by a field-independent mass anisotropy parameter γ_{eff} when the anisotropic Ginzburg–Landau scaling law is applied [81, 82]. This effective anisotropy can be extracted from a plot of $J_c(\theta, B)$ versus the effective field $B_{eff} = \varepsilon(\theta)B$, where $\varepsilon(\theta) = [\cos^2(\theta) + \gamma_{eff}^2 \sin^2(\theta)]^{1/2}$ and γ_{eff} is the mass anisotropy ratio. Concomitantly to the results previously observed in solution derived nanocomposite YBCO thin films (ss- and pn-nanocomposites), here we also observe a strong influence of the nanoparticles on the isotropic pinning contribution. A scaling of the $J_c(\theta, B)$ measurements reported in figure 9(b) for a YBCO–BaZrO₃ nanocomposite (see figure 9(c)) leads to a strong reduction in the effective mass anisotropy, $\gamma_{eff} \sim 2.5$, as compared to $\gamma_{eff} \sim 5$ for pristine YBCO [27, 45, 81, 82]. The reduced effective anisotropy in solution derived YBCO nanocomposites has been associated with the generation of isotropic nanostrain and a novel depairing mechanism generated by tensile strain fields in partial dislocations surrounding the stacking faults [27, 36, 39], so we suggest that a similar vortex pinning landscape exists in the present pn-nanocomposites.

The success in improving the superconducting performance when the nanocomposite film thickness is increased can be better monitored by displaying the corresponding $I_c(B)$ curves. Figure 10 displays such results at 77 K and 5 K for $B//c$ in pristine and pn-nanocomposite films described in previous sections. From these results it becomes clear that a strong enhancement of the superconducting performances has been achieved by increasing the film thickness and by introducing the preformed BaMO₃ ($M = \text{Zr, Hf}$) nanoparticles. For instance, $I_c(B)$ was found to increase by a factor 12 at $B \sim 9$ T and 5 K (or at 3 T and 77 K), in a 20% mol BaZrO₃ nanocomposite film (700 nm thick), as compared to a pristine YBCO thin film with a thickness of 250 nm. The results reported here with the novel colloidal solution processing methodology have demonstrated a strong potential for CCs with enhanced performance; however, further development is still required to achieve the best properties achieved so far in nanocomposite CCs [86, 87].

In conclusion, our measurements of the superconducting properties of YBCO pn-nanocomposite films and coated conductors derived from colloidal solutions of preformed BaMO₃ ($M = \text{Zr, Hf}$) nanoparticles have shown that a strong vortex pinning enhancement can be achieved in addition to the growth of thick YBCO films with controlled nanostructures. This novel approach appears, therefore, to have a strong potentiality for fine tuning of the vortex pinning landscape focusing towards enhanced superconducting

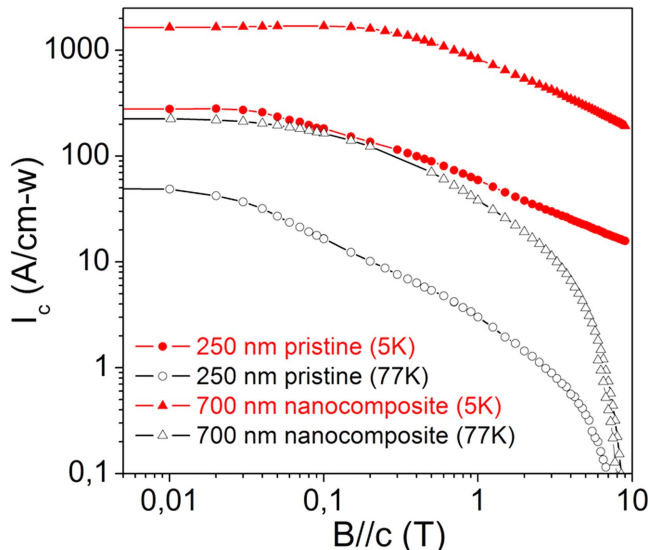


Figure 10. Magnetic field dependence of the total critical current $I_c(B)$ of a nanocomposite thick film (~ 700 nm) of low-fluorine YBCO–BaZrO₃ (20% mol BaZrO₃) compared with pristine YBCO films with thickness of 250 nm. The measurements were performed by electrical transport at 5 K and 77 K, as indicated.

performances in CSD films and thick coated conductors at low cost. A thorough analysis of the potentiality of this approach, as compared to other growth techniques, should be carried out in the future.

4. Conclusions and outlook

Understanding the vortex pinning landscape of superconducting nanocomposite films and coated conductors to be able to optimize their performances requires developing methodologies where the APC and the defect structure can be finely tuned. CSD based YBCO nanocomposite films have been shown to display very appealing performance but it appeared problematic to achieve a tight control of the nanoparticle size and distribution at high nanoparticle concentrations.

The colloidal solution approach to superconducting nanocomposite films has appeared as a very promising route to generate high critical current superconductors because one can separate the two main steps of the process: nanoparticle preparation and YBCO epitaxial thin film growth, provided one can properly avoid the reactivity of the preformed nanoparticles during YBCO growth. The attractiveness of the pn-nanocomposite approach arises from the possibility to separately design the nanoscale features required to achieve efficient artificial pinning centers. This general scheme, however, faced up to several practical difficulties because all along the different steps of the process it became critical to keep a homogeneous distribution of the nanoparticles, to preserve their size and shape and, finally, to generate an optimized nanostructure on the superconducting films. In this work we report very significant progress to achieve these

challenges when we use, as preformed nanoparticles BaMO₃ ($M = \text{Zr}, \text{Hf}$) perovskites that are non-reactive with the Y, Ba and Cu precursors leading to YBCO. These nanoparticles have been prepared as stable solutions following a solvothermal synthesis approach. The nanoparticles are found to be well dispersed in alcoholic media forming stable colloidal solutions that lead to high quality nanocomposite YBCO films, even at nanoparticle concentrations in the range 20%–25% mol, significant progress as compared to previously reported solution derived superconducting ss-nanocomposites.

Furthermore, the nanoparticle size and homogeneity distribution within the films are essentially preserved at high concentrations and when YBCO thick films are grown ($\sim 0.8 \mu\text{m}$). No remarkable nanoparticle coarsening is observed while a high quality YBCO film texture is kept. IJP colloidal solution deposition has been shown to be a versatile and practical deposition approach to form thick YBCO nanocomposite films. This approach has strong capabilities for further enhancement of the film thickness for long length production of coated conductors at low cost. We demonstrated that the pn-nanocomposite films and coated conductors (^{CSD}CZO/^{ABAD}YSZ/SS templates) derived from low-fluorine colloidal solutions display very attractive superconducting performance, both at self-field ($I_c = 220 \text{ A/cm-w}$ at 77 K in thin films) and under high magnetic fields (smoothed $J_c(B)$ magnetic field dependences at 77 K and 5 K). Our STEM analysis of the nanostructure in the films and coated conductors assesses that a high concentration of planar defects parallel to *ab* planes (stacking faults) is achieved, increasing the nanostrain in the films and leading to improved vortex pinning capabilities of the pn-nanocomposite films and coated conductors.

Acknowledgments

All authors acknowledge the EU (EU-FP7 NMP-LA-2012-280432 EUROTAPES project), MINECO (COACHSUPERENERGY, MAT2014-51778-C2-1-R and SUPERINKS, RTC-2015-3640-3) and Generalitat de Catalunya (2014SGR 753 and Xarmae). ICMAB authors acknowledge the Center of Excellence award Severo Ochoa SEV-2015-0496. TEM microscopy work was conducted in the Catalan Institute of Nanoscience and Nanotechnology (ICN2). Authors acknowledge the ICN2 Electron Microscopy Division for offering access to their instruments and expertise. Part of the STEM microscopy work was conducted in ‘Laboratorio de Microscopias Avanzadas’ at the Instituto de Nanociencia de Aragón-Universidad de Zaragoza. Authors acknowledge the LMA-INA for offering access to their instruments and expertise. JG and MC also acknowledge the Ramon y Cajal program (RYC-2012-11709 and RYC-2013-12448, respectively). ZL and BM acknowledge the China Scholarship Council (CSC) and F I MINECO for fellowships, respectively.

ORCID iDs

X Obradors  <https://orcid.org/0000-0003-4592-7718>
A Palau  <https://orcid.org/0000-0002-2217-164X>

References

- [1] MacManus-Driscoll J L, Foltyn S R, Jia Q X, Wang H, Serquis A, Civale L, Maiorov B, Hawley M E, Maley M P and Peterson D E 2004 *Nat. Mater.* **3** 439
- [2] Kang S et al 2006 *Science* **311** 1911
- [3] Shiohara Y, Taneda T and Yoshizumi M 2012 *Jpn. J. Appl. Phys.* **51** 010007
- [4] Malozemoff A P 2012 *Annu. Rev. Mater. Res.* **42** 373
- [5] Obradors X and Puig T 2014 *Supercond. Sci. Technol.* **27** 044003
- [6] Iijima Y, Tanabe N, Kohno O and Ikeno Y 1992 *Appl. Phys. Lett.* **60** 769
- [7] Norton D P, Goyal A, Budai J D and Christen D K 1996 *Science* **274** 755
- [8] Larbalestier D, Gurevich A, Feldmann D M and Polyanskii A 2001 *Nature* **414** 368
- [9] MacManus-Driscoll J L, Zerrer P, Wang H, Yang H, Yoon J, Fouchet A, Yu R, Blamire M G and Jia Q 2008 *Nat. Mater.* **7** 314
- [10] Maiorov B, Baily S A, Zhou H, Ugurlu O, Kennison J A, Dowden P C, Holesinger T G, Foltyn S R and Civale L 2009 *Nat. Mater.* **8** 398
- [11] Matsumoto K and Mele P 2010 *Supercond. Sci. Technol.* **23** 014001
- [12] Obradors X, Puig T, Ricart S, Coll M, Gazquez J, Palau A and Granados X 2012 *Supercond. Sci. Technol.* **25** 123001
- [13] Selvamanickam V et al 2013 *Supercond. Sci. Technol.* **26** 035006
- [14] Wee S H, Gao Y, Zuev Y L, More K L, Meng J, Zhong J, Stocks G M and Goyal A 2012 *Adv. Funct. Mater.* **23** 1912
- [15] Zhao R et al 2014 *Adv. Funct. Mater.* **24** 5240
- [16] Baca F J, Haugan T J, Barnes P N, Holesinger T G, Maiorov B, Lu R, Wang X, Reichart J N and Wu J Z 2013 *Adv. Funct. Mater.* **23** 4826
- [17] Miura S, Yoshida Y, Ichino Y, Xu Q, Matsumoto K, Ichinose A and Awaji S 2016 *APL Mater.* **4** 016102
- [18] Obradors X et al 2006 *Supercond. Sci. Technol.* **19** S13
- [19] Malozemoff A P et al 2008 *Supercond. Sci. Technol.* **21** 034005
- [20] Martin W R et al 2010 *Supercond. Sci. Technol.* **23** 014015
- [21] Izumi T et al 2009 *Physica C* **469** 1322
- [22] Yamada Y and Marchionini B 2015 HTS Roadmap for Electric Power Systems International Energy Agency report <https://iea.org/media/impag/HighTemperatureSuperconductivityARoadmapfortheElectricPowerSectorFINALExecSum.pdf>
- [23] Matias V and Hammond R H 2012 *Phys. Proc.* **36** 1440
- [24] Nakaoka K, Yoshizumi M, Usui Y, Izumi T and Shiohara Y 2014 *Phys. Proc.* **58** 134
- [25] Gutierrez J et al 2007 *Nat. Mater.* **6** 367
- [26] Holesinger T G et al 2008 *Adv. Mater.* **20** 391
- [27] Llordés A et al 2012 *Nat. Mater.* **11** 329
- [28] Coll M, Guzmán R, Gazquez J, Ye S, Puig T and Obradors X 2014 *Supercond. Sci. Technol.* **27** 044008
- [29] Coll M, Ye S, Rouco V, Palau A, Guzman R, Gazquez J, Arbiol J, Suo H, Puig T and Obradors X 2013 *Supercond. Sci. Technol.* **26** 015001
- [30] Engel S, Thersleff T, Huhne R, Schultz L and Holzapfel B 2007 *Appl. Phys. Lett.* **90** 102505
- [31] Miura M, Yoshizumi M, Izumi T and Shiohara Y 2010 *Supercond. Sci. Technol.* **23** 014013
- [32] Cayado P, Erbe M, Kauffmann-Weiss S, Bühler C, Jung A, Häniisch J and Holzapfel B 2017 *Supercond. Sci. Technol.* **30** 094007
- [33] Detavernier C, Özcan A, Jordan-Sweet J, Stach E, Tersoff J, Ross F and Lavoie C 2003 *Nature* **426** 641
- [34] Solano E, Geenen F, Puig T, Obradors X, Mocuta C and Detavernier C 2017 *Thin Sol. Films* **638** 105
- [35] Gazquez J et al 2016 *Adv. Sci.* **3** 1500295
- [36] Guzmán R, Gazquez J, Mundet B, Coll M, Obradors X and Puig T 2017 *Phys. Rev. Mater.* **1** 024801
- [37] Zhang W et al 2007 *IEEE Trans. Appl. Supercond.* **17** 3347
- [38] Yamasaki H, Ohki K, Yamada H, Nakagawa Y and Mawatari Y 2008 *Supercond. Sci. Technol.* **21** 125011
- [39] Deutscher G 2012 *J. Appl. Phys.* **111** 112603
- [40] Koshelev A, Sadovskyy I, Phillips C and Glatz A 2016 *Phys. Rev. B* **93** 060508
- [41] Kwok W-K, Welp U, Glatz A, Koshelev A E, Kihlstrom K J and Crabtree G W 2016 *Rep. Prog. Phys.* **79** 116501
- [42] Horita H, Teranishi R, Yamada K, Kaneko K, Sato Y, Otaguro K, Nishiyama T, Izumi T and Awaji S 2017 *Supercond. Sci. Technol.* **30** 025022
- [43] Miura M et al 2017 *NPG Asia Mater.* **9** e447
- [44] Nakaoka K, Yoshida R, Kimura K, Kato T, Usui Y, Izumi T and Shiohara Y 2017 *Supercond. Sci. Technol.* **30** 055008
- [45] Cayado P et al 2015 *Supercond. Sci. Technol.* **28** 124007
- [46] De Keukeleere K et al 2016 *Adv. Electron. Mater.* **2** 1600161
- [47] Bartolomé E et al 2017 *Adv. Electron. Mater.* **3** 1700037
- [48] Solano E et al 2012 *J. Nanopart. Res.* **14** 1034
- [49] De Keukeleere K, De Roo J, Lommens P, Martins J C, Van Der Voort P and Van Driessche I 2015 *Inorg. Chem.* **54** 3469
- [50] Meledin A, Turner S, Cayado P, Mundet B, Solano E, Ricart S, Ros J, Puig T, Obradors X and Van Tendeloo G 2016 *Supercond. Sci. Technol.* **29** 125009
- [51] De Keukeleere K et al 2017 *Chem. Mater.* **29** 6104
- [52] Miura M, Maiorov B, Willis J O, Kato T, Sato M, Izumi T, Shiohara Y and Civale L 2013 *Supercond. Sci. Technol.* **26** 035008
- [53] Van Driessche I et al 2012 *Supercond. Sci. Technol.* **25** 065017
- [54] Palmer X et al 2016 *Supercond. Sci. Technol.* **29** 024002
- [55] Bartolomé E et al 2013 *Supercond. Sci. Technol.* **26** 125004
- [56] Gerbec J A, Magana D, Washington A and Strouse G F 2005 *J. Am. Chem. Soc.* **127** 15791
- [57] Deshmukh R and Niederberger M 2017 *Chem. Eur. J.* **23** 8542
- [58] Bretos I, Schneller T, Falter M, Backer M, Hollmann E, Wordenweber R, Molina-Luna L, Van Tendeloo G and Eibl O 2015 *J. Mater. Chem. C* **3** 3971
- [59] De Keukeleere K, Feys J, Meire M, De Roo J, De Buysser K, Lommens P and Van Driessche I 2013 *J. Nanopart. Res.* **15** 2074
- [60] De Roo J, Coucke S, Rijckaert H, De Keukeleere K, Sinnaeve D, Hens Z, Martins J C and Van Driessche I 2016 *Langmuir* **32** 1962
- [61] Roma N, Morlens S, Ricart S, Zalamova K, Moreto J M, Pomar A, Puig T and Obradors X 2006 *Supercond. Sci. Technol.* **19** 521
- [62] Usoskin A, Betz U, Hofacker F, Dietrich R and Schlenga K 2017 *IEEE Trans. Appl. Supercond.* **27** 6600605
- [63] Usoskin A and Kirchhoff L 2009 *Mater. Res. Soc. Symp. Proc.* **1150** 117
- [64] Llordés A, Zalamova K, Ricart S, Palau A, Pomar A, Puig T, Hardy A, Van Bael M K and Obradors X 2010 *Chem. Mater.* **22** 1686

- [65] Coll M, Gazquez J, Huhne R, Holzapfel B, Morilla Y, Garcia-Lopez J, Pomar A, Sandiumenge F, Puig T and Obradors X 2009 *J. Mater. Res.* **24** 1446
- [66] Obradors X *et al* 2012 *Physica C* **482** 58
- [67] Zalamova K *et al* 2006 *Chem. Mater.* **18** 5897
- [68] Bean C P 1962 *Phys. Rev. Lett.* **8** 250
- [69] Chen D X and Goldfarb R B 1989 *J. Appl. Phys.* **66** 2489
- [70] Cayado P *et al* 2017 *Supercond. Sci. Technol.* **30** 125010
- [71] Solovyov V, Dimitrov I K and Li Q 2013 *Supercond. Sci. Technol.* **26** 013001
- [72] Granozio F M, Salluzzo M, di Uccio U S, Maggio-Aprile I and Fischer O 2000 *Phys. Rev. B* **61** 756
- [73] Solovyov V F, Wiesmann H J and Suenaga M 2005 *Supercond. Sci. Technol.* **18** 239
- [74] Chen H, Zalamova K, Pomar A, Granados X, Puig T and Obradors X 2010 *Supercond. Sci. Technol.* **23** 034005
- [75] MacManus-Driscoll J, Bravman J and Beyers R 1995 *Physica C* **241** 401
- [76] Sánchez-Valdés C F, Puig T and Obradors X 2015 *Supercond. Sci. Technol.* **28** 024006
- [77] Feenstra R, List F A, Li X, Rupich M W, Miller D J, Maroni V A, Zhang Y, Thompson J R and Christen D K 2009 *IEEE Trans. Appl. Supercond.* **19** 3131
- [78] Wesolowski D E and Cima M J 2007 *J. Mater Res.* **22** 1077
- [79] Solovyov V F *et al* 2014 *Sci. Rep.* **4** 4627
- [80] Palau A *et al* 2018 *Supercond. Sci. Technol.* **31** 034004
- [81] Blatter G, Feigel'man M V, Geshkenbein V B, Larkin A I and Vinokur V M 1994 *Rev. Mod. Phys.* **66** 1125
- [82] Civale L *et al* 2004 *Appl. Phys. Lett.* **84** 2121
- [83] Civale L *et al* 2004 *Physica C* **412–414** 976
- [84] Palau A, Durrell J H, MacManus-Driscoll J L, Harrington S, Puig T, Sandiumenge F, Obradors X and Blamire M G 2006 *Phys. Rev. Lett.* **97** 257002
- [85] Rouco V, Palau A, Guzman R, Gazquez J, Coll M, Obradors X and Puig T 2014 *Supercond. Sci. Technol.* **27** 125009
- [86] Xu A *et al* 2014 *APL Mater.* **2** 046111
- [87] Xu A *et al* 2017 *Sci. Rep.* **7** 6853